1692 Vol. 65, No. 6 / 20 February 2026 / Applied Optics

applied optics

High-efficiency generation of Bessel–Gaussian vortex beams using Bessel-phase-embedded fork-shaped holograms

Ali Mohammad Khazaei,[1] Saifollah Rasouli,[2,3] Sergey A. Ponomarenko,[4,5] and Davud Hebri[5,*]

[1]Department of Physics, Lorestan University, Khorramabad, Iran
[2]Department of Physics, Institute for Advanced Studies in Basic Sciences (IASBS), 444 Prof. Yousef Sobouti Blvd, Zanjan 45137-66731, Iran
[3]Optics Research Center, Institute for Advanced Studies in Basic Sciences (IASBS), Zanjan 45137-66731, Iran
[4]Department of Electrical and Computer Engineering, Dalhousie University, Halifax, Nova Scotia B3J 2X4, Canada
[5]Department of Physics and Atmospheric Science, Dalhousie University, Halifax, Nova Scotia B3H 4R2, Canada
*d.hebri@dal.ca

Received 29 October 2025; revised 13 January 2026; accepted 19 January 2026; posted 20 January 2026; published 9 February 2026

In this paper, we present a high-efficiency protocol for constructing pure amplitude and phase Bessel-phase-embedded fork-shaped holograms to generate Bessel–Gaussian vortex (BGV) beams. When illuminated with a Gaussian beam, these holograms produce BGV beams in the first diffraction orders. To quantify the performance of the generated beams, we introduce a quality factor that measures the degree of similarity between the generated BGV beam and an ideal BGV beam. Our results demonstrate that the proposed holograms achieve a significantly higher level of similarity compared to the conventional method of generating BGV beams, which involves the sequential use of a spiral phase plate (SPP) and an axicon or their equivalent computer-generated holograms. Additionally, we compare the diffraction efficiency of BGV beams generated using our approach for both pure amplitude and phase holograms. Phase holograms are implemented using a spatial light modulator (SLM), whereas pure amplitude holograms are printed on sheet glass or plastic substrates. The use of pure amplitude holograms offers a highly efficient, cost-effective, and straightforward method for generating BGV beams, making them an attractive alternative to traditional techniques.

https://doi.org/10.1364/AO.581634

1. INTRODUCTION

One of the well-known solutions to the scalar Helmholtz equation in free space is the family of zero-order Bessel beams, first introduced by Durnin in 1987 [1]. These optical beams, characterized by a transverse amplitude profile governed by the Bessel function of the first kind, exhibit the remarkable property of propagating without diffraction. In other words, the intensity pattern of the beam remains unchanged during free-space propagation, making them ideal for applications requiring long-range beam stability.

Various methods have been developed to generate such non-diffracting Bessel beams, including Fabry–Perot resonators [2], axicons [3], computer-generated holograms (CGHs) [4,5], leaky-wave modes [6], phase plates [7], and near-field plates [8]. The unique propagation invariance of Bessel beams has led to their widespread application in areas such as stable optical trapping and manipulation of metallic nanoparticles [9], advanced microscopy [10], and ultrafast laser material processing [11]. These applications highlight the importance of developing efficient and practical methods for generating such beams.

Higher-order Bessel beams (HOBBs), unlike their zero-order counterparts, exhibit a vortex-like structure with a helical phase front and a null intensity at the beam center. These vortex beams have extended relevance in both classical and emerging domains such as quantum optics and nonlinear photonics. Variants like vector Bessel beams with spatially varying polarization and HOBBs carrying orbital angular momentum (OAM) have opened up new avenues in optical and quantum communications [12–14].

Despite their doughnut-shaped intensity profiles, HOBBs retain the essential features of non-diffraction and self-healing. The OAM of such beams is intrinsically linked to their azimuthal phase distribution [15]. The self-healing property enables the beam to reconstruct its shape after encountering an obstacle, a capability of particular importance for applications in optical micromanipulation and biophotonic workstations, where robust propagation through scattering environments is essential [16–18].

Beam generation techniques for HOBBs are generally categorized into active and passive approaches [19]. Active methods involve direct transformation of Gaussian or plane waves within cylindrical waveguides or resonators to produce high-order Bessel–Gaussian (BG) beams [19]. In contrast, passive methods typically convert pre-existing beams into BG vortex beams using optical elements such as spiral phase plates or axicons [15].

In this work, we propose a high-efficiency method for generating Bessel–Gaussian vortex (BGV) beams using pure amplitude and phase fork-shaped holograms that encode Bessel-phase structures. When illuminated by a Gaussian beam, these holograms generate BGV beams in the first diffraction orders. To evaluate the fidelity of the generated beams, we introduce a quality factor that quantifies the similarity between the generated and ideal BGV beams.

Our findings demonstrate that the proposed holograms outperform traditional methods—such as sequential use of a spiral phase plate and an axicon, or their equivalent holograms—in terms of beam quality. Furthermore, we compare the diffraction efficiency of amplitude and phase holograms. While phase holograms are implemented using a spatial light modulator (SLM), pure amplitude holograms are fabricated on glass or plastic substrates. The latter offer a cost-effective and efficient alternative for practical BGV beam generation.

2. FREE SPACE PROPAGATION OF A BESSEL–GAUSS VORTEX BEAM

A celebrated ideal Bessel vortex beam withstands free space diffraction. We can express its complex amplitude in cylindrical coordinates (r, θ, z) as

$$u(\mathbf{r}, z) = J_l(k_r r)\exp[i(l\theta + k_z z)], \tag{1}$$

where $\mathbf{r} = (x, y) = (r\cos\theta, r\sin\theta)$ is the position vector in the transverse plane, J_l is an lth order Bessel function of the first kind, and order l. Further, k_r and k_z are the radial and longitudinal components of the wave vector. Here we define a characteristic length d_0 so that $k_r = \frac{2\pi}{d_0}$. As an ideal Bessel beam carries infinite power, in practice only Bessel–Gauss vortex (BGV) beams can be realized in the laboratory. The field profile of any BGV in the source plane has the form [20,21]:

$$u_{\mathrm{BGV}}(\mathbf{r}, 0) = J_l(k_r r)\exp\left(-r^2/w_g^2 + il\theta\right), \tag{2}$$

where w_g is the beam waist of the Gaussian envelope. Free space evolution of any BGV obeys the Fresnel integral:

$$u_{\mathrm{BGV}}(\mathbf{r}, z) = \left(\frac{k}{2\pi iz}\right)\int \mathrm{d}\mathbf{r}' u_{\mathrm{BGV}}(\mathbf{r}', 0)e^{ik|\mathbf{r}-\mathbf{r}'|^2/(2z)}, \tag{3}$$

where $k = \sqrt{k_r^2 + k_z^2} = \frac{2\pi}{\lambda}$ is the light's wave number. On substituting Eq. (2) in (3), performing the angular integration with the aid of the integral representation of J_l, we arrive at

$$u_{\mathrm{BGV}}(\mathbf{r}, z) = \frac{kh(-i)^{l+1}}{z} \times e^{il\theta}\int_0^\infty J_{|l|}(k_r r')J_{|l|}\left(krr'/z\right) \times e^{-r'^2\left(w_g^{-2} - i\frac{k}{2z}\right)} r'\mathrm{d}r', \tag{4}$$

where $h = e^{ik(z+\frac{r^2}{2z})}$ and we used $J_{-m}(x) = (-1)^m J_m(x)$. We can now evaluate the radial integral with the aid of [22]

$$\int_0^\infty \mathrm{d}x x e^{-\rho^2x^2} J_l(ax)J_l(bx) = \frac{1}{2\rho^2}\exp\left(-\frac{a^2+b^2}{4\rho^2}\right) I_l\left(\frac{ab}{2\rho^2}\right), \tag{5}$$

yielding, after straightforward algebra, the expression

$$u_{\mathrm{BGV}}(\mathbf{r}, z) = \frac{(-i)^{l+1}hz_R}{z - iz_R}e^{il\theta}e^{-\frac{w_g^2\left(k_r^2 + k^2r^2/z^2\right)}{4(1-iz_R/z)}} I_{|l|}\left(\frac{k_r z_R r}{z - iz_R}\right). \tag{6}$$

Here $z_R = kw_g^2/2$ is a Rayleigh range of the Gaussian envelope. Using Eq. (6), the evolution of two BGV beams with $l = \pm 2$, $\lambda = 532$ nm, $w_g = 2.5$ mm, and $d_0 = 0.5$ mm under propagation from $z = 0$ to $z = 10$ m are presented in Visualization 1. In order to demonstrate the mathematical consistency of Eq. (6) with established formulations in the literature, we examine the far-field propagation limit. It follows at once from Eq. (6) that in the far-field propagation limit, $z \gg z_R$, we have

$$u(\mathbf{r}, z) = \frac{(-i)^{l+1}hz_R}{z}e^{il\theta}e^{-\frac{w_g^2\left(k_r^2 + k^2r^2/z^2\right)}{4}} I_{|l|}\left(\frac{k_r z_R r}{z}\right). \tag{7}$$

Given that the Fourier transform of a BGV beam results in a perfect vortex (PV) beam [21], and considering the connection between far-field diffraction and Fourier transform, we anticipate that Eq. (7) will have the form of a PV beam. Upon comparing Eq. (7) with Eq. (3) in [23], we observe that it resembles a PV beam characterized by a ring thickness of $T = \frac{2z}{kw_g}$ and a ring radius of $R = \frac{k_r z}{k}$. Clearly, the radius of the intensity ring is directly proportional to the propagation distance z, implying that the area of the intensity pattern scales proportionally to z^2. Conversely, the intensity peak diminishes by a factor of z^{-2}. Therefore, in practice, a Fourier lens is employed to transform a BGV beam into a PV beam instead of relying on free space propagation.

3. CONSTRUCTING HOLOGRAMS FOR BESSEL–GAUSSIAN VORTEX BEAMS GENERATION

Holography includes the capturing and reconstruction of optical waves. A hologram is a 2D transparent sheet that encodes the information of an original wave's intensity and phase. To create a hologram, we need to combine a known reference wave with the original wave and capture how they interfere with each other on the $z = 0$ plane. By choosing a plane wave that its wavevector locates in the $x - z$ plane making an angle φ with z axis as a reference wave, the transmittance of the hologram can be written as [24]

$$t(\mathbf{r}) \propto 1 + I_0 + 2\sqrt{I_0}\cos\left(\frac{2\pi}{\Lambda}x - \phi_0\right), \tag{8}$$

where I_0 and ϕ_0 are the intensity and phase of the original wave at $z = 0$ plane, respectively, and $\Lambda = \lambda/\sin\varphi$. Illuminating this hologram with a plane wave, the complex amplitude of the diffracted light, $\psi(\mathbf{r}, z)$, can be expressed as

$$\psi(\mathbf{r}, z) \propto FR_z\{c(\mathbf{r})\} + FR_z\left\{\sqrt{I_0}e^{i(k_x x - \phi_0)}\right\} + FR_z\left\{\sqrt{I_0}e^{-i(k_x x - \phi_0)}\right\}, \tag{9}$$

where $FR_z\{\}$ denotes Fresnel propagator, $c(\mathbf{r}) = 1 + I_0$, and $k_x = \frac{2\pi}{\Lambda}$. The first term, $FR_z\{c(\mathbf{r})\}$, signifies the zero-order diffraction, while the remaining two terms represent the original beams over the first diffraction orders. As is apparent, the functionality of $c(\mathbf{r})$ does not impact the generated original beams. Therefore, for the sake of simplicity, we can set $c(\mathbf{r})$ as a constant. Consequently, the modified version of Eq. (8) is

$$t(\mathbf{r}) \propto \mathrm{C} + 2\sqrt{I_0}\cos\left(\frac{2\pi}{\Lambda}x - \phi_0\right), \tag{10}$$

where C is a constant. We generate a hologram to create a BGV beam using the abovementioned method. For this purpose, we consider an ideal Bessel beam as the original wave. Then, by setting $z = 0$ in Eq. (1), we get $I_0 = J_l^2(k_r r)$ and $\phi_0 = l\theta$. Substituting these values in Eq. (10) we get

$$t_{\mathrm{Am}}(\mathbf{r}) = \frac{1}{2}\left[1 + \frac{J_l(k_r r)}{a_l}\cos(k_x x - l\theta)\right] = \frac{1}{2}\left[1 + g_l(\mathbf{r})\right], \tag{11}$$

where a_l represents the first peak of the function $J_l(x)$. The proportionality constant has been chosen so that $t(\mathbf{r})$ is confined between 0 and 1. Moreover, $g_l(\mathbf{r}) = \frac{J_l(k_r r)}{a_l}\cos(k_x x - l\theta)$ fluctuates between -1 and $+1$. Figure 1 shows the transmittance of some pure amplitude holograms, defined by Eq. (11), with different TCs.

Now, let us examine the pure phase hologram pattern achievable using a spatial light modulator (SLM). This type of hologram does not absorb light, resulting in a power transmittance of unity. The transmittance for the phase hologram can be determined by

$$t_{\mathrm{Ph}}(\mathbf{r}) = \exp\left[i\gamma g_l(\mathbf{r})/2\right], \tag{12}$$

where γ is the phase depth of the hologram so that the phase alternates between $-\gamma/2$ and $+\gamma/2$. By substituting $g_l(\mathbf{r})$ and using Jacobi–Anger expansion

$$e^{ix\cos(\alpha)} = J_0(x) + 2\sum_{m=1}^{\infty} i^m J_m(x)\cos(m\alpha). \tag{13}$$

Equation (12) can be rewritten as follows:

$$t_{\mathrm{Ph}}(\mathbf{r}) = J_0(\chi) + 2iJ_1(\chi)\cos\left(k_x x - l\theta\right) + \ldots, \tag{14}$$

where $\chi = \frac{\gamma J_l(k_r r)}{2a_l}$. It should be mentioned that the first term, $J_0(\chi)$, represents the zero-order diffraction, the second term represents the first diffraction orders that are supposed to generate the desired BGV beam, and higher-order terms represent the higher diffraction orders. For $\chi \le 1$, we have $J_1(\chi) \approx \frac{\chi}{2}$, see Fig. 3 of [25]. As $\frac{J_l(k_r r)}{a_l} \le 1$ and $\gamma \le 2\pi$, the condition is most likely to be satisfied for most values of r and we can write

$$t_{\mathrm{Ph}}(\mathbf{r}) \approx J_0(\chi) + i\gamma\frac{J_l(k_r r)}{2a_l}\cos(k_x x - l\theta) + \ldots. \tag{15}$$

Comparing Eqs. (15) and (11) shows that the pure phase and pure amplitude holograms approximately have the same form. We can use the following unified form for the transmittance of amplitude and phase holograms:

$$t(\mathbf{r}) = t_0 + t_1\sum_{m=\pm 1} J_l(k_r r)\exp[im(k_x x - l\theta)], \tag{16}$$

where $t_0 = \frac{1}{2}$ and $t_1 = \frac{1}{4a_l}$ for amplitude hologram expressed by Eq. (11), and $t_0 = J_0(\chi)$ and $t_1 = \frac{i\gamma}{2a_l}$ for phase hologram expressed by Eq. (15).

When the above-presented holograms are illuminated with a Gaussian beam, $u_G(\mathbf{r}, 0) = \exp(-r^2/w_g^2)$ we show that the first diffraction orders will form a BGV beam. The complex amplitude of the diffracted light immediately after the hologram is

$$\psi(\mathbf{r}, 0) = t(\mathbf{r})\exp\left(-r^2/w_g^2\right). \tag{17}$$

By substituting $t(\mathbf{r})$ Eq. (16) in Eq. (17) and using Fresnel propagator integral, Eq. (3), we get

$$\psi(\mathbf{r}, z) = FR_z\{\psi(\mathbf{r}, 0)\} = u_0(\mathbf{r}, z) + t_1\sum_{m=\pm 1} u_m(\mathbf{r}, z), \tag{18}$$

where $u_0(\mathbf{r}, z) = FR_z\{t_0\exp(-r^2/w_g^2)\}$ generally and $u_0(\mathbf{r}, z) = t_0 u_G(\mathbf{r}, z)$ when t_0 is a constant in which $u_G(\mathbf{r}, z)$ is the well-known propagation of a Gaussian beam. Further, $u_m(\mathbf{r}, z)$ is obtained as

$$u_m(\mathbf{r}, z) = \left(\frac{kh}{2\pi iz}\right)\int \mathrm{d}\mathbf{r}' e^{-r'^2\left(w_g^{-2} - i\frac{k}{2z}\right) - i\frac{k}{z}\left(x_m x' + y y'\right) - ilm\theta'} J_l(k_r r'), \tag{19}$$

where $x_m = x - m\frac{\lambda z}{\Lambda}$ is the transferred coordinate to the center of mth diffraction order. Let us define $r_m = \sqrt{x_m^2 + y^2}$ and $\theta_m = \tan^{-1}(\frac{y}{x_m})$ as the polar coordinates around the center of mth diffraction order. Substituting $(x_m, y) = (r_m\cos\theta_m, r_m\sin\theta_m)$ and $(x', y') = (r'\cos\theta', r'\sin\theta')$ in Eq. (19), and utilizing the integral representation of J_l we get

$$u_m(\mathbf{r}, z) = \frac{(-i)^{l+1}kh}{z}e^{-iml\theta_m}\int_0^\infty J_{|l|}(k_r r')J_{|l|}\left(kr_m r'/z\right) \times e^{-r'^2\left(w_g^{-2} - i\frac{k}{2z}\right)} r'\mathrm{d}r'. \tag{20}$$

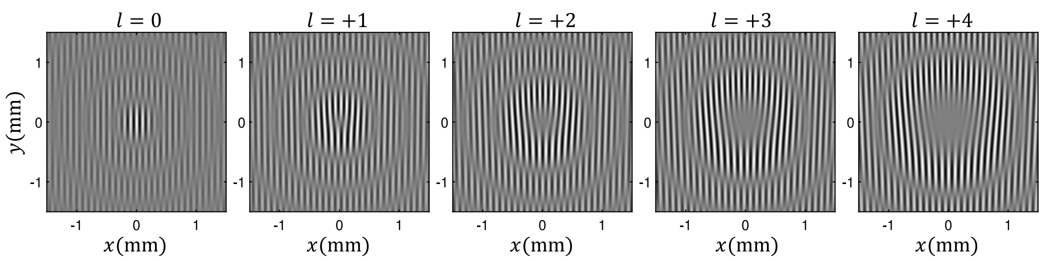

Fig. 1. Transmittance of some pure amplitude holograms with $\Lambda = 0.1$ mm and $d_0 = 1$ mm for generating BGV beams with different TCs.

By using the integral Eq. (5), Eq. (20) reduces to

$$u_m(\mathbf{r}, z) = \frac{(-i)^{l+1} h z_R}{z - i z_R} e^{-iml\theta_m - \frac{w_g^2 \left(k_r^2 + k^2 r_m^2 / z^2\right)}{4(1 - i z_R / z)}} I_{|l|}\left(\frac{k_r z_R r_m}{z - i z_R}\right). \tag{21}$$

When we compare Eqs. (21) and (6), we observe that the first diffraction orders align with the typical pattern of a BGV beam. This alignment holds for an amplitude hologram, yielding an exact result. However, for the phase holograms, it is an approximation. Notably, once a sufficient distance has been covered from the hologram, allowing the different diffraction orders to separate adequately, we can place a Fourier lens along the pathway of the first diffraction order to produce a PV.

In Fig. 2, these features are verified by simulation of the diffraction of a Gaussian beam from some designed holograms. The first column of Fig. 2, first to third rows, shows the generated BGV beams over the first diffraction orders of a Gaussian beam diffracted from amplitude (first row) and phase (second and third rows). The entire diffraction pattern evolution under propagation from $z = 0$ to $z = 3$ m is illustrated in Visualization 2. For the amplitude hologram, it is evident that the power contribution of the zero-diffraction order is higher than that of the first orders, and the maximum intensity is observed at the location of the zero-diffraction order (see the color scale to the right). However, the intensity profiles of the generated and ideal BGV beams exhibit full compatibility. Moreover, by comparing the second and third rows, we observe that increasing the phase depths from $\gamma = \pi$ to $\gamma = 2\pi$ results in a significant increase in the power contribution of the first diffraction orders. However, compatibility between the intensity profiles of the generated and ideal BGV beams declines. The second column shows the normalized intensity profiles of the generated BGV beams compared to the normalized intensity profile of the ideal BGV beam.

The conventional approach to generating a BGV beam involves the sequential use of an SPP and an axicon [15] or equivalent computer-generated holograms [26,27]. Associated transmittance can be expressed as follows:

$$t(\mathbf{r}) = \exp(-ik_r r + il\theta), \tag{22}$$

where $\exp(-ik_r r)$ represents the phase of an axicon and $\exp(il\theta)$ shows the phase of an SPP. By substituting $t(\mathbf{r})$ in Eq. (17) and substituting the result in the Fresnel propagator, Eq. (3), we get

$$\psi(\mathbf{r}, z) = \frac{kh(-i)^{l+1}}{z} e^{il\theta} \int_0^\infty J_l(krr'/z) e^{-ik_r r'} e^{-r'^2\left(w_g^{-2} - i\frac{k}{2z}\right)} r' \mathrm{d}r'. \tag{23}$$

Upon comparing Eqs. (23) and (4), it becomes evident that the resultant light field from transmitting a Gaussian beam

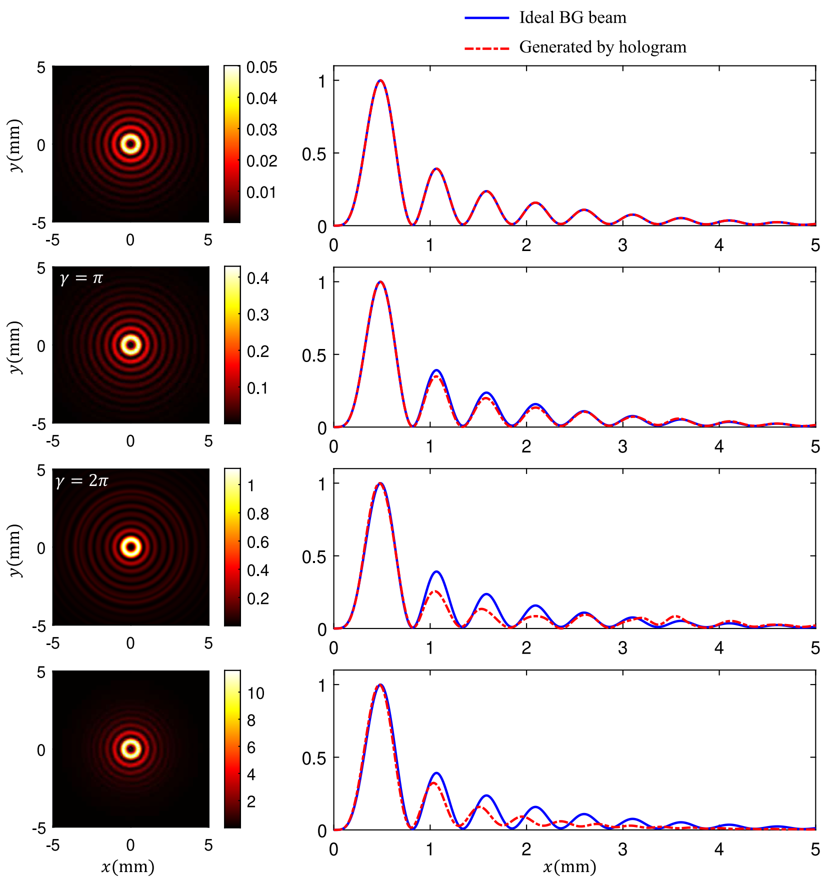

Fig. 2. First column: generated BGV beams by the diffraction of a Gaussian beam having $w_g = 5$ mm and $\lambda = 532$ nm at a distance $z = 3$ m from an amplitude (first row); phase (second and third rows) holograms with $l = 2$, $\Lambda = 0.1$ mm, and $d_0 = 1$ mm; and consecutive SPP and an axicon (fourth row). Second column: normalized intensity profile of the generated BGV beams in the first column (dashed red plot) in comparison with the normalized intensity profile of the ideal BGV beam (solid blue plot). See Visualization 2 and Visualization 3.

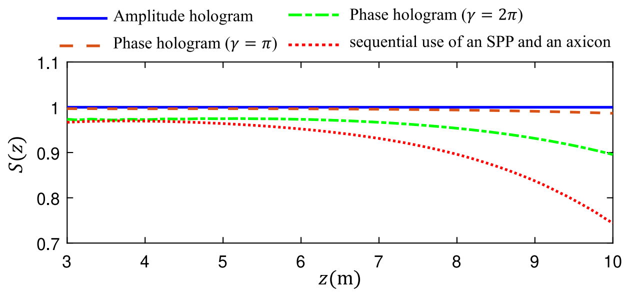

Fig. 3. Degree of similarity between ideal BGV beam and generated BGV beams by different holograms, represented in Fig. 2, in terms of propagation distance.

through consecutive SPP and an axicon, or equivalent holograms, does not precisely match the ideal BGV beam. Using the stationary phase method, Eq. (23) can be analyzed mathematically. The propagation distance over which the diffracted light can be approximated with a BGV beam can be estimated geometrically to be $z_{\max} = w_g k/k_r$. The last row of Fig. 2 and Visualization 3 correspond to the diffraction of a Gaussian beam from a transmittance represented by Eq. (22).

We use the following degree of similarity to quantify the quality of the generated BGV beams [28]:

$$S(z) = \frac{\int_0^\infty I(r,z) I_0(r,z) \mathrm{d}r}{\int_0^\infty I^2(r,z)\mathrm{d}r + \int_0^\infty I_0^2(r,z)\mathrm{d}r - \int_0^\infty I(r,z) I_0(r,z)\mathrm{d}r}, \tag{24}$$

where $I_0(r,z)$ and $I(r,z)$ are normalized intensity profiles of the ideal and generated BGV beams. Figure 3 illustrates the degree of similarity between the ideal BGV beam and the beams generated by various holograms as a function of propagation distance, calculated using Eq. (24). As is apparent, the level of similarity achieved by the holograms proposed in this study surpasses the similarity achieved by consecutive SPP and an axicon, or an equivalent hologram.

4. EXPERIMENTS AND RESULTS

To experimentally validate some of the theoretical results presented above, we illuminate amplitude and phase holographic structures using a collimated Gaussian beam. In these structures, the phase of the Bessel function is embedded into the phase of a forked grating. The amplitude holograms, featuring sinusoidal and binary profiles with various topological charges (TCs), were fabricated using a lithographic method on plastic sheets. Additionally, phase holograms were generated using a spatial light modulator (SLM) extracted from an LCD projector (3M X50, resolution: 1024 × 768, display: 0.7 in. polysilicon LCD), where the phase modulation was constrained to $\gamma = \pi/2$. The experimental setup employs the second harmonic of an Nd:YAG diode laser (wavelength $\lambda = 532$ nm) with a Gaussian beam profile, which is collimated using a spatial filter and a positive lens. The collimated beam then illuminates the amplitude and phase holograms, and the resulting diffraction patterns are recorded at various distances using a Nikon D7200 camera.

Figure 4 provides a schematic of the experimental setup, categorizing the holograms into four distinct groups: (a) sinusoidal amplitude, (b) binary amplitude, (c) sinusoidal phase, and (d) binary phase. This setup enables a comparative analysis of how different holographic structures influence diffraction patterns, offering insights into their optical behavior under Gaussian beam illumination. The SLM used in this study has a pixelated structure, which is effectively equivalent to a 2D orthogonal pure phase binary structure, see [29] and Appendix C of [30]. This inherent texture leads to undesired diffraction of the incident beam across a two-dimensional array, even without the application of an arbitrary phase distribution. When a phase distribution is imposed on the SLM, it generates a two-dimensional array of modulated beams. Since all diffraction orders produced by the SLM share identical properties, we only allow the central diffraction order to propagate. The remaining diffraction orders are blocked using a spatial mask, as depicted in Fig. 4

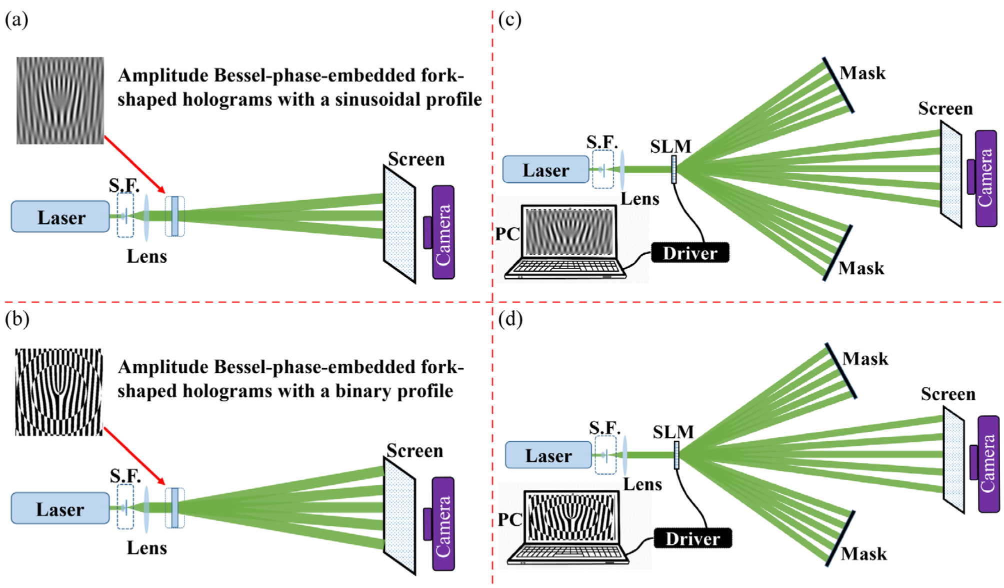

Fig. 4. Experimental setup for the diffraction of a Gaussian beam from holograms with the following profiles: (a) sinusoidal amplitude, (b) binary amplitude, (c) sinusoidal phase, and (d) binary phase.

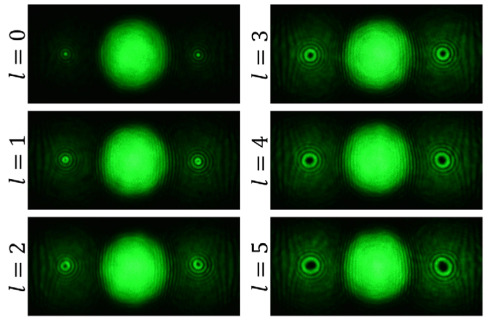

Fig. 5. Experimental diffraction patterns of a Gaussian beam passing through amplitude structures with a sinusoidal profile, where the baseline forked grating has a period of $\Lambda = 0.3$ mm and topological charges ranging from 0 to 5. The patterns were recorded at a distance of $z = 665$ cm using a camera equipped with an imaging lens.

Figure 5 shows the experimental diffraction patterns of a Gaussian beam passing through amplitude structures with a sinusoidal profile, where the baseline forked grating has a period of $\Lambda = 0.3$ mm and topological charges ranging from 0 to 5. These patterns were formed on a screen and recorded using a camera equipped with an imaging lens at a distance of $z = 665$ cm. For sinusoidal amplitude structures, three primary diffraction orders are observed: the central order, along with the first positive and first negative orders. The central diffraction order corresponds to the Gaussian beam (with zero topological charge), while the positive and negative diffraction orders correspond to Gaussian–Bessel beams carrying positive and negative topological charges, respectively. As the structure parameter l increases, the topological charge of the generated Bessel vortex beam also increases. The distinct variations in the diffraction patterns arise due to differences in the topological charge.

Figure 6 shows the experimental diffraction patterns of a Gaussian beam passing through amplitude structures with a binary profile, where the forked grating has a period of $\Lambda = 0.2$ mm and its topological charges ranging from 0 to 5. These patterns were recorded at a distance of $z = 645$ cm using the same camera used in Fig. 5. For binary amplitude structures, the observed diffraction orders include the central order, first positive and negative orders, and two higher orders. The first positive and first negative diffraction orders exhibit higher intensity compared to higher-order diffractions.

Table 1 shows power ratios measured using a power meter (Coherent LMP10i Laser Detector) for binary amplitude structures with different topological charges. First, the laser beam power was measured before illuminating the structures. Then, the power was recorded immediately after the structures and, as shown in Fig. 4, at a specific distance where the diffraction orders were spatially separated. The power of each diffraction order was individually measured at this stage.

According to Table 1, the power shares of the first positive and negative diffraction orders are approximately twice that of the second positive and negative diffraction orders. The laser beam power before reaching the grating, measured directly without a lens, is 0.175 W. Due to the high intensity, a neutral density filter was used to reduce the beam power.

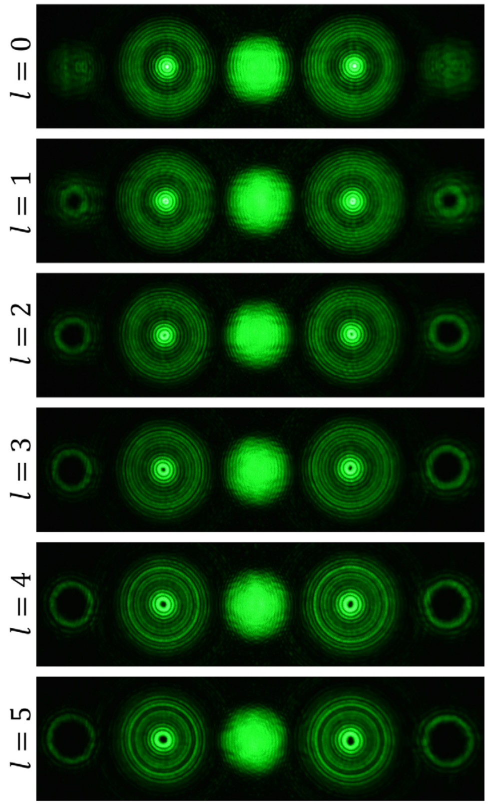

Fig. 6. Experimental diffraction patterns of a Gaussian beam passing through binary amplitude structures with a forked grating ($\Lambda = 0.2$ mm) and topological charges from 0 to 5, recorded at $z = 645$ cm. The first positive and negative diffraction orders exhibit higher intensity, and their topological charge increases with the structure parameter l.

Table 1. Experimentally Measured Power Ratios, Calculated as the Sum of the Intensity Values for Each Diffraction Order Relative to the Total Intensity of the Entire Diffraction Pattern Shown in Fig. 6

$m =$	$m = -2$	$m = -1$	$m = 0$	$m = 1$	$m = 2$	
			$\frac{P_m}{P_i}$			
$l =$	$\frac{P_{-2}}{P_i}$%	$\frac{P_{-1}}{P_i}$%	$\frac{P_0}{P_i}$%	$\frac{P_1}{P_i}$%	$\frac{P_2}{P_i}$%	$\frac{\sum_{m=-2}^{+2} P_m}{P_i}$%
0	9.8	20.1	40.2	20.2	9.7	95
1	10.1	20.3	39.3	20.2	10.1	95.4
2	10.4	20.1	38.9	20.2	10.4	95.6
3	10.7	19.7	39.1	19.9	10.6	95.3
4	10.6	19.9	39.4	19.8	10.5	94.5
5	10.7	19.6	39.5	19.6	10.6	94.1

Approximately 28.5% of the incident beam intensity passes through the binary amplitude structure. Since these structures contain opaque (black) regions, they do not allow all the incident light to pass through.

Figure 7 shows the experimental diffraction patterns of a Gaussian beam passing through phase structures with a sinusoidal profile, where the grating has a period of $\Lambda = 0.11$ mm and topological charges ranging from 0 to 5. These patterns were recorded at a distance of $z = 338$ cm using a camera equipped with an imaging lens.

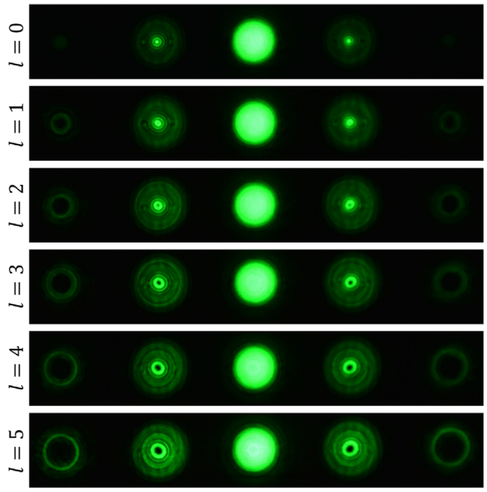

Fig. 7. Experimental diffraction patterns of a Gaussian beam passing through sinusoidal phase structures with a grating period of $\Lambda = 0.11$ mm and topological charges ranging from 0 to 5, recorded at $z = 338$ cm. The phase modulation depth is $\gamma = \pi/2$. The first positive and negative diffraction orders exhibit higher intensity, and their topological charge increases with the structure parameter l.

Table 2. Experimentally Measured Power Ratios, Calculated as the Sum of the Intensity Values for Each Diffraction Order Relative to the Total Intensity of the Entire Diffraction Pattern Shown in Fig. 7

$m =$	$m = -2$	$m = -1$	$m = 0$	$m = 1$	$m = 2$	
			$\frac{P_m}{P_i}$			
$l =$	$\frac{P_{-2}}{P_i}\%$	$\frac{P_{-1}}{P_i}\%$	$\frac{P_0}{P_i}\%$	$\frac{P_1}{P_i}\%$	$\frac{P_2}{P_i}\%$	$\frac{\sum_{m=-2}^{+2} P_m}{P_i}\%$
0	0.2	0.4	98.8	0.4	0.2	95.07
1	0.5	0.55	97.9	0.55	0.5	94.84
2	0.57	0.78	97.3	0.78	0.57	94.4
3	0.64	0.96	96.8	0.96	0.64	94.47
4	0.64	1.12	96.48	1.12	0.64	94.15
5	0.67	1.24	96.18	1.24	0.67	93.95

Table 2 shows the power shares measured for sinusoidal phase structures with different topological charges. The laser beam power was first measured immediately after passing through the structures. Then, as shown in Fig. 4, the power of each diffraction order was recorded at a specific distance where the diffraction orders were spatially separated.

The laser beam power before reaching the SLM was measured to be 0.670 W.

The laser beam power after passing through the SLM (measured by placing the power meter directly at the output):

- SLM off: 0.642 W
- SLM on, without a diffraction pattern: 0.613 W.

The power of each diffraction order was measured as

- SLM off: 93.3 mW; SLM on, without a diffraction pattern: 89 mW

Similarly, Fig. 8 shows the diffraction patterns of a Gaussian beam passing through phase structures with a binary profile, using the same parameters as in Fig. 7. The patterns were captured on a screen using a camera with an imaging lens.

In both Figs. 7 and 8, the phase modulation depth of the spatial light modulator is set to $\gamma = \pi/2$. For both sinusoidal and binary phase structures, the observed diffraction orders include the central order, first positive and negative orders, and higher orders. The first positive and first negative diffraction orders exhibit higher intensity compared to the higher-order diffractions.

Table 3 shows the power shares measured for binary phase structures with different topological charges. The laser beam power was first measured immediately after passing through the structures.

Figure 9 shows the experimental diffraction patterns of a Gaussian beam passing through sinusoidal phase structures with a forked grating with a period of $\Lambda = 0.11$ mm, a fixed topological charge of 3, and characteristic lengths of 0.4, 0.6,

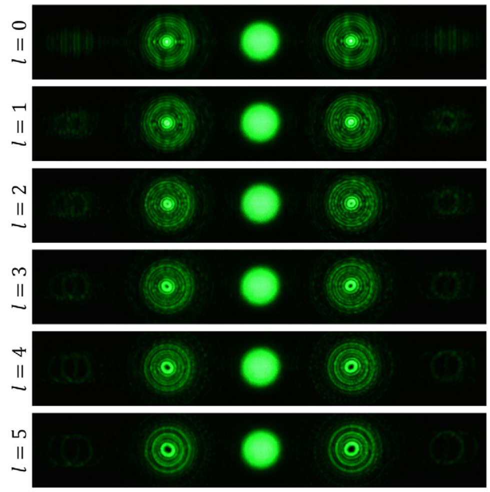

Fig. 8. Experimental diffraction patterns of a Gaussian beam passing through binary phase structures, using the same parameters as in Fig. 7. The patterns were recorded at $z = 338$ cm with a phase modulation depth of $\gamma = \pi/2$. The first positive and negative diffraction orders show higher intensity, and their topological charge increases with the structure parameter l.

Table 3. Experimentally Measured Power Ratios, Calculated as the Sum of the Intensity Values for Each Diffraction Order Relative to the Total Intensity of the Entire Diffraction Pattern Shown in Fig. 8

$m =$	$m = -1$	$m = -1$	$m = 0$	$m = 1$	$m = 2$	
			$\frac{P_m}{P_i}$			
$l =$	$\frac{P_{-2}}{P_i}\%$	$\frac{P_{-1}}{P_i}\%$	$\frac{P_0}{P_i}\%$	$\frac{P_1}{P_i}\%$	$\frac{P_2}{P_i}\%$	$\frac{\sum_{m=-2}^{+2} P_m}{P_i}\%$
0	1.96	6.09	83.9	6.09	1.96	92.07
1	1.92	6.15	83.86	6.15	1.92	91.57
2	1.91	6.12	83.94	6.12	1.91	91.34
3	1.93	6.10	83.94	6.10	1.93	91.31
4	1.94	6.33	83.46	6.33	1.94	91.55
5	1.94	6.34	83.44	6.34	1.94	91.59

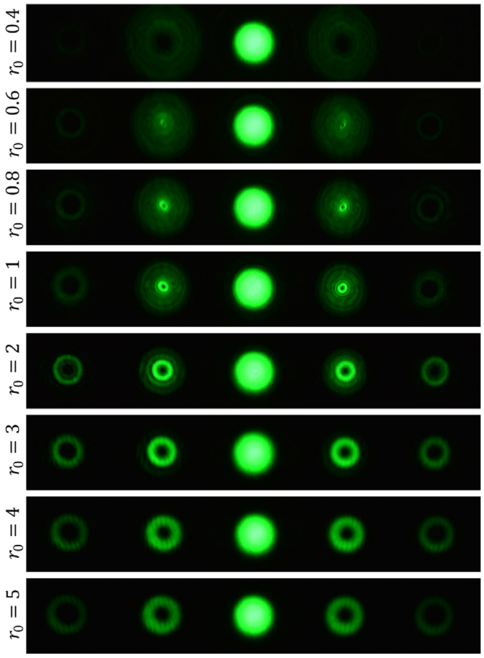

Fig. 9. Experimental diffraction patterns of a Gaussian beam passing through sinusoidal phase structures with a forked grating ($\Lambda = 0.11$ mm), a fixed topological charge of 3, and characteristic lengths ranging from 0.4 to 5. The patterns were recorded at $z = 340$ cm using a camera with an imaging lens.

0.8, 1, 2, 3, 4, and 5. These patterns were recorded at a distance of $z = 340$ cm using a camera equipped with an imaging lens.

Similar to Figs. 7 and 8, these phase structures exhibit a central diffraction order, as well as first and second positive and negative diffraction orders. The first positive and first negative diffraction orders show higher intensity compared to the higher-order diffractions.

For sinusoidal phase structures, an increase in the characteristic length results in an expansion of the dark central region of the Bessel vortex beams observed in the first positive and first negative diffraction orders.

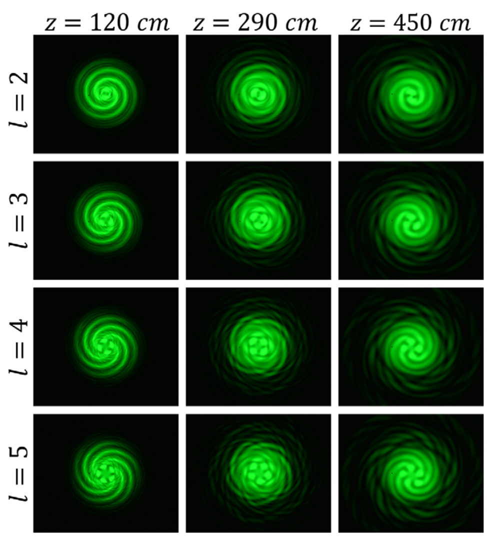

Fig. 10. Experimental diffraction patterns of gratings formed by the superposition of vortex and axicon phases, recorded directly on the camera sensor at different propagation distances. This approach facilitates the generation of high-order Bessel vortex beams using high-level phase holograms.

Figure 10 shows the experimental diffraction patterns of gratings generated by the superposition of a vortex phase and an axicon phase. The diffraction patterns of these gratings, which have different topological charges, were recorded directly on the camera sensor without a lens at various propagation distances. This method enables the generation of high-order Bessel vortex beams using high-level phase holograms, as demonstrated in [27].

5. CONCLUSION

In this study, we introduced and analyzed a novel method for generating Bessel–Gaussian vortex (BGV) beams using pure amplitude and phase Bessel-phase-embedded fork-shaped holograms. Our findings indicate that these holograms provide superior beam quality compared to conventional approaches, as quantified by a newly defined quality factor. Furthermore, the diffraction efficiency analysis confirms that the proposed method is highly effective for both amplitude and phase holograms.

The practical implementation of our approach demonstrates distinct advantages, particularly in the case of pure amplitude holograms, which can be fabricated on low-cost substrates such as glass and plastic sheets. This makes them an accessible and efficient alternative for applications requiring high-quality BGV beams without the need for expensive phase modulation devices.

Overall, our work paves the way for more efficient and cost-effective holographic techniques in beam shaping, with potential applications in optical trapping, laser processing, and microscopy. Future research may explore optimizing the design parameters of these holograms to further enhance beam quality and extend their applicability to broader optical systems.

Funding. Institute for Advanced Studies in Basic Sciences (G2025IASBS12632); Iran National Science Foundation (4037535); Natural Sciences and Engineering Research Council of Canada (NSERC) (RGPIN-2018-05497).

Acknowledgment. The author Davud Hebri would like to acknowledge Izaak Walton Killam Postdoctoral fellowship.

Disclosures. The authors declare no conflicts of interest.

Data availability. Data underlying the results presented in this paper are not publicly available at this time but may be obtained from the authors upon reasonable request.

REFERENCES

1. J. Durnin, "Exact solutions for nondiffracting beams. I. the Scalar theory," J. Opt. Soc. Am. A **4**, 651–654 (1987).
2. A. J. Cox and D. C. Dibble, "Nondiffracting beam from a spatially filtered Fabry–Perot resonator," J. Opt. Soc. Am. A **9**, 282–286 (1992).
3. G. Indebetouw, "Nondiffracting optical fields: some remarks on their analysis and synthesis," J. Opt. Soc. Am. A **6**, 150–152 (1989).
4. J. Turunen, A. Vasara, and A. T. Friberg, "Holographic generation of diffraction-free beams," Appl. Opt. **27**, 3959–3962 (1988).
5. J. Salo, J. Meltaus, E. Noponen, *et al.*, "Millimetre-wave Bessel beams using computer holograms," Electron. Lett. **37**, 834–835 (2001).

6. M. Ettorre and A. Grbic, “Generation of propagating Bessel beams using leaky-wave modes,” IEEE Trans. Antennas Propag. **60**, 3605–3613 (2012).
7. M. E. Terzi, S. A. Tsysar, P. V. Yuldashev, *et al.*, “Generation of a vortex ultrasonic beam with a phase plate with an angular dependence of the thickness,” Mosc. Univ. Phys. Bull. **72**, 61–67 (2017).
8. M. F. Imani and A. Grbic, “Generating evanescent Bessel beams using near-field plates,” IEEE Trans. Antennas Propag. **60**, 3155–3164 (2012).
9. G. Rui, X. Wang, and Y. Cui, “Manipulation of metallic nanoparticle with evanescent vortex Bessel beam,” Opt. Express **23**, 25707–25716 (2015).
10. F. O. Fahrbach, P. Simon, and A. Rohrbach, “Microscopy with self-reconstructing beams,” Nat. Photonics **4**, 780–785 (2010).
11. R. Stoian, M. K. Bhuyan, G. Zhang, *et al.*, “Ultrafast Bessel beams: advanced tools for laser materials processing,” Adv. Opt. Technol. **7**, 165–174 (2018).
12. D. McGloin and K. Dholakia, “Bessel beams: diffraction in a new light,” Contemp. Phys. **46**, 15–28 (2005).
13. X. Chu, Q. Sun, J. Wang, *et al.*, “Generating a Bessel-Gaussian beam for the application in optical engineering,” Sci. Rep. **5**, 18665 (2015).
14. M. McLaren, T. Mhlanga, M. J. Padgett, *et al.*, “Self-healing of quantum entanglement after an obstruction,” Nat. Commun. **5**, 3248 (2014).
15. J. Arlt and K. Dholakia, “Generation of high-order Bessel beams by use of an axicon,” Opt. Commun. **177**, 297–301 (2000).
16. X. Chu, “Analytical study on the self-healing property of Bessel beam,” Eur. Phys. J. D **66**, 259 (2012).
17. V. Garcés-Chávez, K. Dholakia, and G. C. Spalding, “Extended-area optically induced organization of microparticles on a surface,” Appl. Phys. Lett. **86**, 031106 (2005).
18. M. Mousavi, H. Nadgaran, and S. Salimian, “High-power transverse mode selection of Bessel–Gaussian beams,” Appl. Phys. B **127**, 66 (2021).
19. V. S. Ilchenko, M. Mohageg, A. A. Savchenkov, *et al.*, “Efficient generation of truncated Bessel beams using cylindrical waveguides,” Opt. Express **15**, 5866–5871 (2007).
20. F. Gori, G. Guattari, and C. Padovani, “Bessel-Gauss beams,” Opt. Commun. **64**, 491–495 (1987).
21. P. Vaity and L. Rusch, “Perfect vortex beam: Fourier transformation of a Bessel beam,” Opt. Lett. **40**, 597–600 (2015).
22. D. Zwillinger and A. Jeffrey, *Table of Integrals, Series, and Products* (Elsevier, 2007).
23. J. Pinnell, V. Rodríguez-Fajardo, and A. Forbes, “How perfect are perfect vortex beams?” Opt. Lett. **44**, 5614–5617 (2019).
24. B. E. Saleh and M. C. Teich, *Fundamentals of Photonics* (John Wiley & Sons, 2019).
25. M. Zarei, D. Hebri, and S. Rasouli, “1D spatially chirped periodic structures: managing their spatial spectrum and investigating their near-field diffraction,” J. Opt. Soc. Am. A **39**, 2354–2375 (2022).
26. C. Paterson and R. Smith, “Higher-order Bessel waves produced by axicon-type computer-generated holograms,” Opt. Commun. **124**, 121–130 (1996).
27. Z. Zhai, J. Huang, Z. Cheng, *et al.*, “Realizing high-order bessel vortex beams with high-level phase holograms,” IOP Conf. Ser. Mater. Sci. Eng. **569**, 032039 (2019).
28. J. C. Yue and M. K. Clayton, “A similarity measure based on species proportions,” Commun. Stat. - Theory Methods **34**, 2123–2131 (2005).
29. S. Rasouli and A. M. Khazaei, “An azimuthally-modified linear phase grating: generation of varied radial carpet beams over different diffraction orders with controlled intensity sharing among the generated beams,” Sci. Rep. **9**, 12472 (2019).
30. P. Y. Moghadam, S. Rasouli, F. Hajizadeh, *et al.*, “Three-dimensional optical multiple trapping using pure amplitude octagonal almost periodic structures,” Opt. Express **31**, 43490–43505 (2023).